



POLITECNICO
MILANO 1863

**SCUOLA DI INGEGNERIA INDUSTRIALE
E DELL'INFORMAZIONE**

PROJECT REPORT - AERODYNAMICS OF TRANSPORT VEHICLES

Aerodynamic Analysis of the Interaction between the F1 Front Wing and the Wheel Wake

Author: RATTI ANDREA, RAVANELLI PIETRO, SCHIFONE MARCO

Professors: PROF. PAOLO SCHITO, PROF. LUIGI VIGEVANO

Assistant professor: ING. STEFANO NEGRI

Academic year: 2023-2024

1. Introduction

This study presents an investigation on the aerodynamics of a Formula 1 (F1) front wing and its interaction with wheel wake. The front wing is a crucial component in the aerodynamic design of a F1 car, as it is responsible for the production of a consistent amount of the overall downforce, hence impacting performances and stability of the car. In 2022 the FIA (*Fédération Internationale de l'Automobile*) introduced a new set of technical regulations [1], with the aim of simplifying the aerodynamic design of the cars and boosting overtake possibilities. The key idea was the reintroduction of the ground effect, making the undertray the main source of downforce. The front wing has been simplified and it was removed the gap between the nose and the wing flap, which will be directly connected. Despite the full-width elements providing a greater total wing area, the new design produces less downforce. The regulations allow up to four wing elements (down from five), with their contours tightly defined by the FIA control volumes. This design permits reasonable camber at the inboard ends but tapers to very little camber at the outboard ends. Additionally, the elements are limited in their angle, restricting the overall angle of attack of the wing. The aim of these changes was to simplify the wing's geometry, reducing the turbulent wake produced and decreasing the loss of downforce when cars are following each other closely, enhancing the challenge possibilities between drivers. The new set of regulations have also restricted the capabilities of the teams of controlling the front wheel wake.

1.1. Theoretical Background

Wheels play a crucial role in the overall aerodynamic drag of a Formula 1 car, they produce about 40% of the total drag [2]. Wheels act as bluff bodies, generating large wakes, which can affect in a major way the efficiency of the car if they are not controlled properly. The flow structures that develop around them interact in a complex way with their surroundings, making both experimental and numerical investigations of the flow significantly challenging.

As shown in Figure 1, various vortices occur around a rotating wheel under flow conditions. The most important ones are:

- Wake Horseshoe Vortex: a dominating structure that generates high drag.
- C-Shoulder Vortex Pair: occurs due to flow separation in the upper after part of the tyre, resulting in high lift.
- Symmetric Contact Patch Vortex: this vortex is usually weak.
- Stagnation Point Horseshoe Vortex: this is typically a weak vortex too.

Due to the complexity of this analysis, there are few accepted studies. Notable among them are the experiments conducted by Fackrell and Harvey [3], which investigated both stationary and rotating wheels. Their findings indicated that a rotating wheel results in reduced lift and drag compared to a stationary wheel. Fackrell also discovered that when the wheel is rotating, there is a significant pressure peak upstream of the contact patch, as illustrated in Figure 2. This peak is caused by a phenomenon Fackrell called "jetting" which is provoked by the interaction of the moving ground and the tyre forcing fluid towards the contact patch, resulting in a jet of fluid emerging from the sides of the wheel. Additionally, Fackrell estimated the separation point of the flow: when the wheel is rotating, the flow separates earlier compared to the stationary case, thereby reducing drag for the rotating wheel.

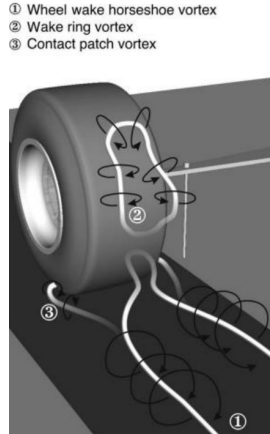


Figure 1: Vortices past a wheel [4].

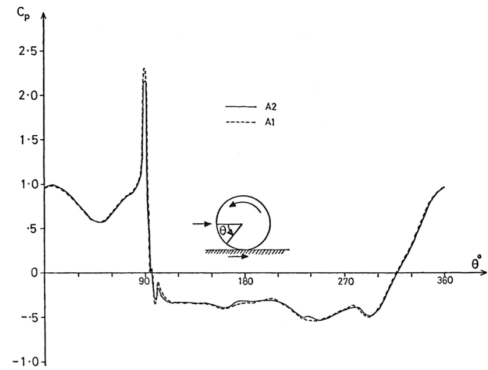


Figure 2: Pressure coefficient along the centerline of the wheel obtained by Fackrell for A1 and A2 tyres [3].

2. CAD

The CAD models used for the simulations have been developed from scratch by means of the software *SolidWorks*. For the isolated wheel analysis, it is designed a simple model of a slick tyre with no rims and grooves, while the contact patch is described in Section 3.2. For the second simulation it is created a multi-element front wing following the 2022 regulations, which imposes strict dimensions of the control volumes where the wing is placed, imposing also constraints on the distance between the wing elements. The wing is composed of four flaps: for the main flap the NACA 4415 is used, while for the other three the NACA 6409 is adopted. It is designed also a nose shape, which length is extended to avoid that the separation at the end of the body affects the results. All of these parts are created separately and then they are assembled, in order to be able to define different surface refinements in the mesh generation procedure. The 3D view of the full model and the most significant dimensions are reported in Figure 3. The frame of reference is placed on the leading edge of the wing on the vertical plane of symmetry of the car. For the purpose of the following study the suspensions are not considered.

flap	chord [mm]	AoA [°]
main	240	1
1	140	22
2	100	30
3	90	38

Table 1: Flap parameters at the root.

flap	chord [mm]	AoA [°]
main	210	1
1	140	4
2	55	7
3	45	10

Table 2: Flap parameters at the tip.

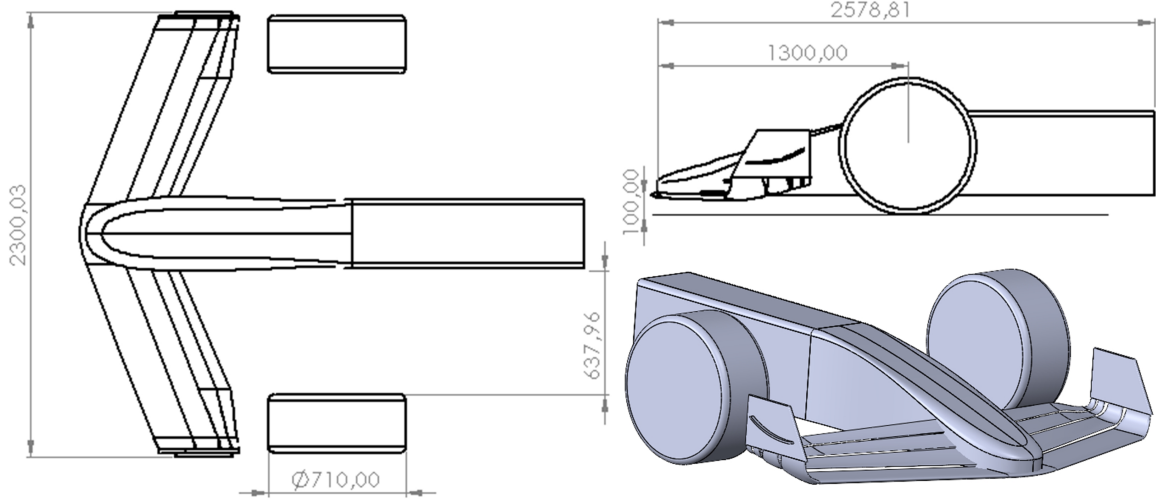


Figure 3: Top, side and isometric view with dimensions in mm.

3. Numerical Setup

In this work, CFD simulations based on Reynolds-Averaged Navier-Stokes equations (RANS) are carried by exploiting the use of *OpenFOAM*, an open-source software. As for the solvers, the PotentialFoam algorithm has been used to initialize the solution with a potential flow solver, the SimpleFoam has been employed to solve the RANS equations. The SIMPLE (Semi-Implicit Method for Pressure Linked Equations) algorithm is used to solve the governing equations for the steady-state, incompressible case since the low Mach number ($M_a = 0.12$) allows this simplification. Moreover, in order to solve the closure problem a turbulence model needs to be selected. For this work the $k - \omega$ SST model is used and detailed informations about it are provided in Section 3.1.

3.1. Turbulence model and boundary conditions

In order to solve the RANS equations, it is necessary to model the term related to the Reynolds stress tensor. This can be done by choosing the turbulence model that is more suitable to the problem. The $k - \omega$ SST model [5], which belongs to the family of the two equations models, has been chosen for this simulation. It has been developed specifically to resolve the flow in problems that involve the presence of adverse pressure gradients and regions of separated flow. The $k - \omega$ SST model allows to blend the standard $k - \omega$ model, which is used in the near wall region, and the $k - \varepsilon$ model, used in the outer region, by means of a specific blending function.

In a CFD simulation, designating the initial and boundary conditions properly is crucial. The initial values of the simulation are shown in Table 3, where I is the turbulence intensity, which has been set to 5% corresponding to a medium-turbulent case, and C_μ is a model constant for the turbulence model.

To ensure that the simulation is a good representation of the real problem, it is necessary to set the proper boundary conditions at the different interfaces. In addition, since it is not feasible to resolve directly the viscous sublayer, which requires a value of $y^+ < 1$, the use of wall functions is exploited. Since only half of the car is simulated, a symmetry boundary condition must be imposed on the symmetry plane, which assumes a zero flux of all the quantities across it. Table 4 shows all the boundary conditions and the wall functions employed in the simulations for the full model case.

$U_\infty [\text{m/s}]$	$p_\infty [\text{Pa}]$	$\omega [1/\text{s}]$	$I [-]$	$\kappa [\text{J/kg}]$	$C_\mu [-]$
40	0	9000	5 %	3.375	0.09

Table 3: Initial values.

Boundary	U	p	ω	κ	ν_t
Car	fixedValue	zeroGradient	omegaWallFunction	kqRWallFunction	nutUSpaldingWallFunction
Tyre	rotatingWallVelocity	zeroGradient	omegaWallFunction	kqRWallFunction	nutUSpaldingWallFunction
Ground	movingWallVelocity	zeroGradient	omegaWallFunction	kqRWallFunction	nutUSpaldingWallFunction
Inlet	fixedValue	zeroGradient	fixedValue	fixedValue	zeroGradient
Outlet	inletOutlet	fixedValue	zeroGradient	zeroGradient	zeroGradient
Sides	slip	slip	slip	slip	slip
Symmetry wall	symmetry	symmetry	symmetry	symmetry	symmetry

Table 4: Boundary conditions.

3.2. Mesh generation

The computational domain is built exploiting the model half symmetry along the median longitudinal plane. The size of the domain is $19\text{ m} \times 4\text{ m} \times 4\text{ m}$, and the model is placed at 4 m from the inlet surface. For the mesh generation phase the *blockMesh* and *snappyHexMesh* tools, available on *OpenFOAM*, are used. The background mesh has cubic cells of size equal to 0.2 m . The computational domain is shown in Figure 4.

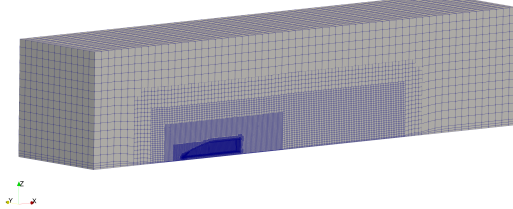


Figure 4: Computational domain.

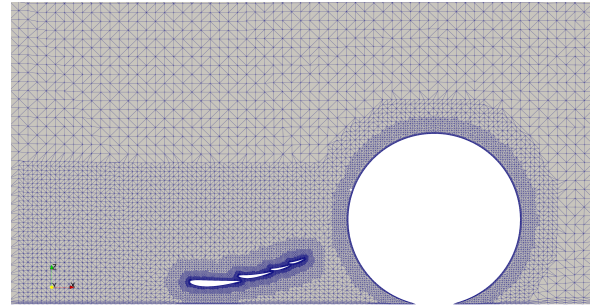


Figure 5: Mesh refinement around the model.

The modelling of the contact patch between tyre and ground is realized by setting the limits of the blockmesh in order to cut a small portion of the lower part of the wheel, to avoid the tangency between tyre and ground; it is arbitrary chosen to make a cut of 5 mm . To ensure accurate and reliable results, a mesh refinement strategy has been implemented. Three refinement boxes are placed, with the last one having a level of refinement equal to 4, which corresponds to cells with the size of 12.5 mm . A further refinement has been applied near the surface of the model, where the geometry is complex and it is crucial to capture the behaviour of the flow. The cells near the wing have the maximum level of refinement of 8, with the dimensions of 1.56 mm . Lastly, it is necessary to add layers near the surfaces in order to capture also the behaviour of the flow in the boundary layer. To achieve this an important parameter to control is y^+ , the non dimensional distance from the wall, defined as follows:

$$y^+ = \frac{yu_\tau}{\nu}$$

$$u_\tau = \sqrt{\frac{\tau_w}{\rho}}$$

where the friction velocity u_τ has been introduced as well. A value of $y^+ < 1$ is required to capture properly the velocity profile and the shear stress in the boundary layer, however this would require a very refined mesh with an excessive number of cells. Hence a higher value of y^+ can be achieved by means of wall functions. The turbulence model adopted, the $k - \omega$ SST, requires a value of $y^+ \approx 10 - 120$, to do so 5 layers have been added to all the model and the ground, with the aim of capturing correctly also the boundary layer developed over the ground surface. The first cell height is set as 0.267 mm and an average value of $y^+ < 60$ is obtained on the whole model. The details of the mesh refinement phase are shown in Figure 5.

3.3. Numerical schemes

In *OpenFOAM*, the numerical schemes are declared in the *fvSchemes* file in the system directory. Second-order accurate schemes have been used for all the quantities in the turbulence equations in order to guarantee stability and convergence. Concerning gradient scheme, the second-order accurate Gauss linear method has been used. For the divergence terms, the linear-upwind scheme, which is a blend of the linear and upwind

schemes (respectively first and second order methods), has been employed, except for the $\text{div}(\phi, U)$ for which a linear scheme was selected. As interpolation scheme, the linear method has been used in order to interpolate the solution from the cell centers to the face centers. Lastly, concerning the Laplacian terms, the Gauss linear scheme is selected.

4. Results

4.1. Convergence

To assess the quality of the simulation, the trend of the initial residuals and of the force coefficients are analysed. First of all, results of the isolated tyre simulation are presented; from Figure 6 it is possible to conclude that after 300 iterations initial residuals tend to stabilize, and similarly, as shown in Figure 7, the values of drag and lift coefficients slightly oscillate around stable values in the last 200 iterations.

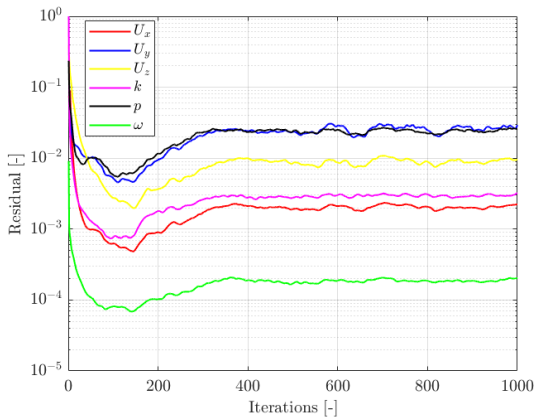


Figure 6: Residuals of isolated tyre.

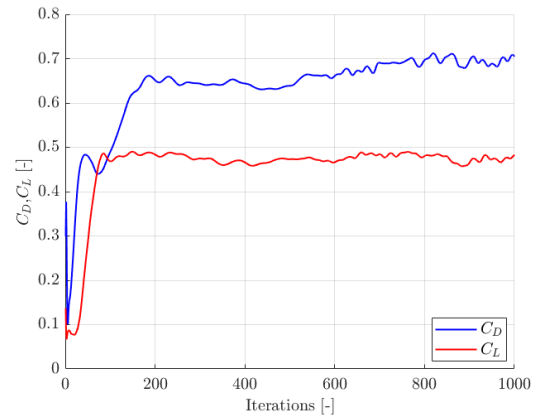


Figure 7: Force coefficients of isolated tyre.

For the full model simulation, initial residual evolution is reported in Figure 8, and global force coefficients are shown in Figure 9. All the residuals are below 10^{-3} and the force coefficients tend to stable values after 500 iterations.

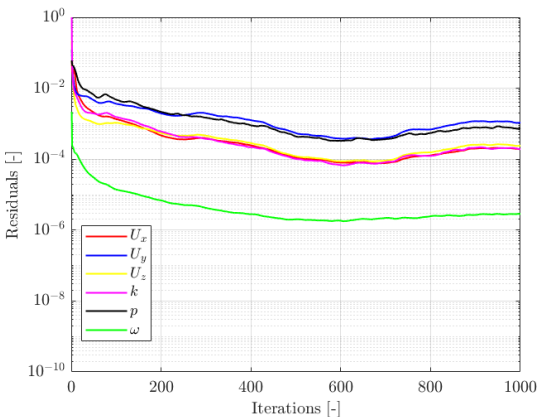


Figure 8: Residuals of full model.

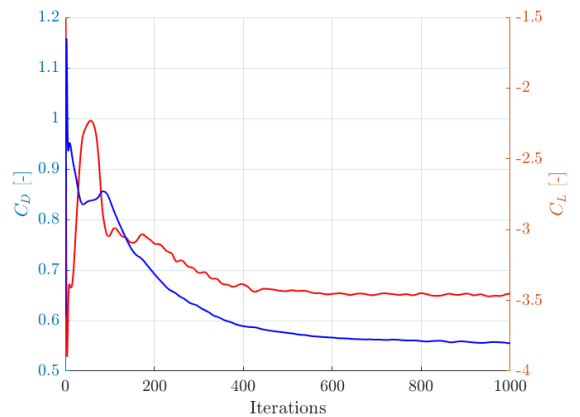


Figure 9: Force coefficients of the full model.

Finally for both the simulations a grid convergence analysis based on the drag coefficient is performed. For the isolated tyre simulation, three different meshes are used with a number of cells approximately of 250 000, 650 000 and 1.6M. From the results presented in Figure 10 and Table 5 it is possible to notice that the error is reduced very quickly as the mesh is refined, the relative error between the medium and fine mesh is below 0.2% and the mesh convergence is achieved. The grid convergence of the full model simulation is verified increasing the number of cells from 1.4M, to 3.8M, to 6.7M, as shown in Figure 11 and Table 6, also in this case the error is relatively small below 1.5%. A further refinement cannot be applied because of the computational cost of the simulation.

	Cells (mln)	C_D	$C_{D_{err}}$
Coarse	0.25	0.7002	5.0790%
Medium	0.65	0.6676	0.1936%
Fine	1.60	0.6630	-

Table 5: Tyre grid convergence relative errors w.r.t. fine mesh.

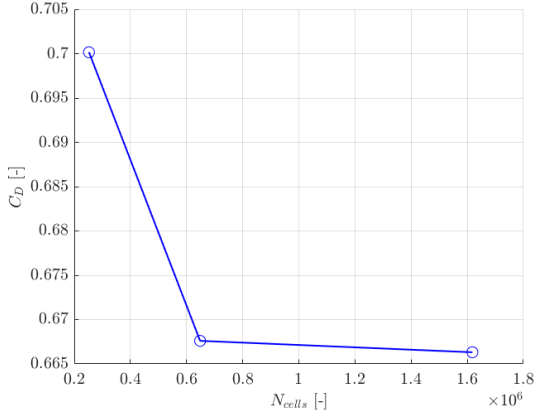


Figure 10: Grid convergence isolated tyre.

	Cells (mln)	C_D	$C_{D_{err}}$
Coarse	1.40	0.7227	8.5302%
Medium	3.80	0.6757	1.4702%
Fine	6.70	0.6659	-

Table 6: Full model grid convergence relative errors w.r.t. fine mesh.

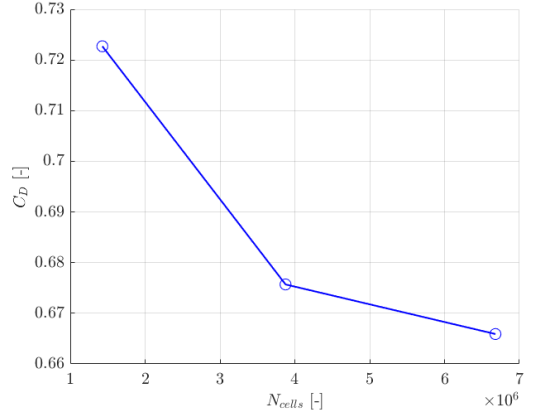


Figure 11: Grid convergence full model.

4.2. Post-processing

As outlined in Section 1 the primary objective is to study the interaction between the front wing and the tyre. To achieve this, it is initially examined the isolated tyre and then it is considered in the analysis also the front wing and the car's nose to observe the differences in terms of flow behaviour and aerodynamic loads in this configuration. It is crucial to underline that in this study only steady-state RANS simulations are carried out, and only a qualitative analysis of the wake and vortices is possible. For a complete and more in-depth analysis of the behavior of the flow, URANS, DES, LES would be required to exploit the unsteady nature of the flow.

4.2.1 Tyre

This initial analysis is crucial for understanding the baseline aerodynamic characteristics of the tyre without the influence of other components. By focusing on the tyre alone, it is possible to identify key features such as pressure distribution, velocity fields and vortex generations.

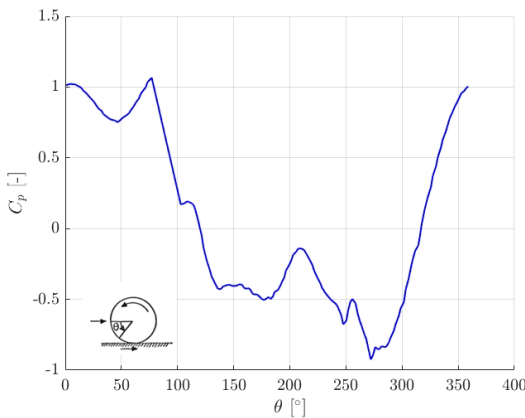


Figure 12: Value of C_P along the centerline of the tyre.

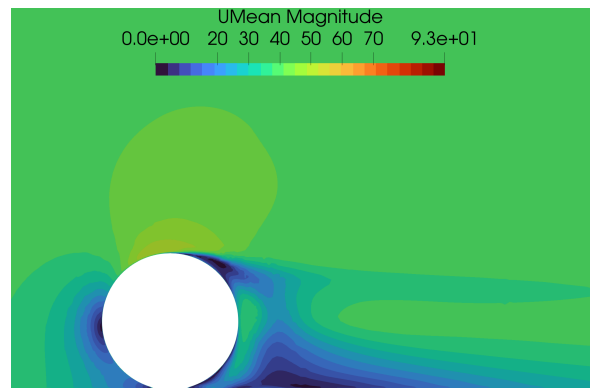


Figure 13: Mean velocity magnitude on the wheel centerline (plane $y = 0.98$ m).

The first result that is presented is the evolution of the pressure coefficient along the centerline of the rotating tyre, depicted in Figure 12. The distribution of C_P matches the experimental results shown in Figure 2, from 0° to 180° and from 270° to 360° . The main discrepancy with numerical results occurs around the separation point, located at 272.09° , where the C_P has its minimum value, hence flow reaches the maximum velocity. The reason behind this disagreement can be found in the unsteady nature of the problem. The results are affected by the type of simulation carried out, in this case a steady RANS simulation is not sufficient for a complete study the behaviour of the wheel wake.

Next, it is analysed the velocity field, as shown in Figure 13. The stagnation point is clearly visible on the left side of the tyre, along with the separation zone at the back of the tyre. This behaviour can be easily explained: as the flow accelerates over the upper part of the tyre, it is created an adverse pressure gradient, leading to flow separation and the formation of vortical structures, which can be seen in Figure 14 where the total pressure coefficient is plotted on the plane $x = 1.7\text{ m}$, located downstream of the tyre. The total pressure coefficient is a non dimensional parameter that translates the energy of the flow relative to the car. It can be also useful to find the presence of vortices in the flow. The C_{Ptot} is defined as P_t/P_{t0} , where P_t is the total pressure in any point and P_{t0} is the reference total pressure, which is the one at the inlet.

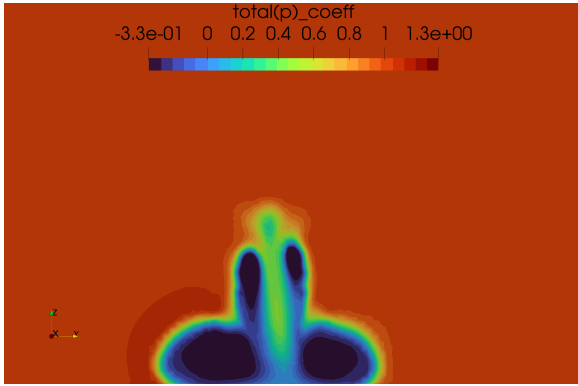


Figure 14: C_{Ptot} at $x = 1.7\text{ m}$.

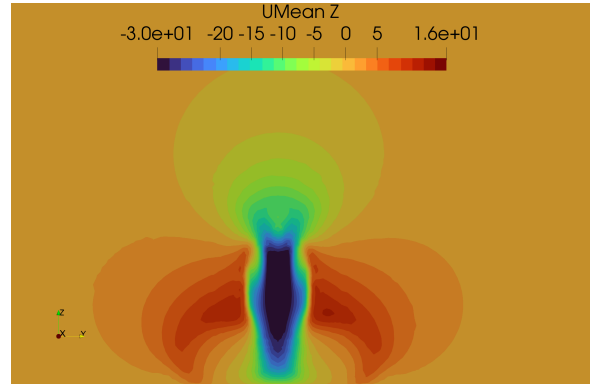


Figure 15: Vertical velocity component at $x = 1.7\text{ m}$.

Figure 14 shows the two pairs of counter-rotating vortices and their induced velocities are the dominant structures in the flow field. The wake of the wheel can be divided into two regions: the upper wake region, where it is located the pair of vortices generated by the tyre shoulders, and the lower wake, where a pair of counter-rotating ground vortices is present. The intensity of the two pairs is comparable. In between the eddies, hence on the midspan of the wheel, the velocity sum up and generate a strong downwash effect, with the effect of pushing the flow towards the ground. This particular behaviour of the flow is clearly visible when the vertical velocity component is plotted, as in Figure 15. The ground vortices are generated in the region close to the contact patch, where the flow is ejected from both the sides of the wheel. This is the jetting phenomenon explained in Section 1.1. Moving downstream, the upper vortices are displaced towards the ground, due to the downwash effect, and merge with the lower wake. Hence, the wake is becoming shorter but also wider in span as the flow moves downstream.

4.2.2 Full model

After studying the isolated tyre, it is analysed the full model, which includes the car's nose, front wing, and tyre. This comprehensive analysis allows to observe and evaluate the differences and interactions between these components, providing a more complete understanding of the vehicle's aerodynamics. The first analysis focuses on the static pressure coefficient to identify areas of high and low pressure around the vehicle, which in turn influences the overall aerodynamic performance, including drag and downforce characteristics. From Figure 16 the stagnation regions on tyre and nose tip are clearly visible.

In Figure 17 it is presented the static pressure coefficient trend on the tyre for the two cases. It is possible to see that its behaviour is similar to the one obtained with the isolated tyre, even though some differences can be highlighted. The stagnation point is now located at $\theta = 8.11^\circ$, which is approximately 4° different from the isolated wheel case. This behaviour can be explained with the influence of the suction side of the wing on the tyre, which is pushing high speed flow towards the wheel, thus changing the aerodynamics of the flow, as shown in Figure 23. In particular the region on the wheel between $\theta = 0^\circ$ and $\theta = 90^\circ$ is affected by the presence

of the wing, and a lower local minimum value of the C_P is present in this region. In addition, the separation point is now located at $\theta = 282.9^\circ$, which is about 10° different from the previous case, due to which separation happens before with respect to the isolated wheel. From previous studies and literature review [6] it has been found that the ride height is a crucial parameter for pressure coefficient and, in particular, for the separation point on a wheel with the presence of an inverted wing. Reducing the ride height, hence the distance of the wing from the ground, can cause the forward shifting of the separation point. Moreover, the ride height has also a major influence on the aerodynamic coefficients of the tyre, due to the different interaction with the vortical structures generated by the wing.

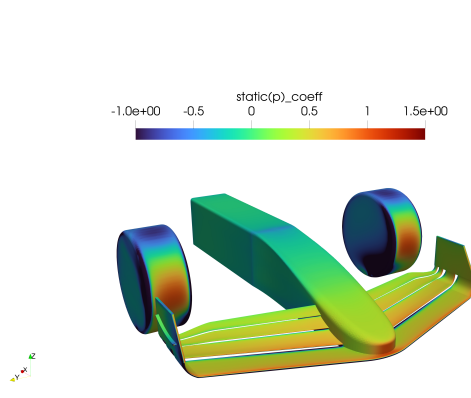


Figure 16: C_P static on the full model.

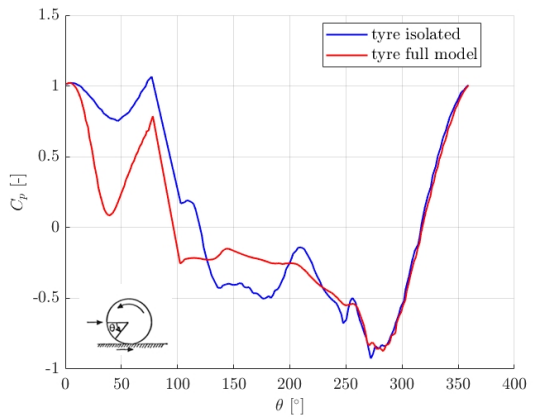


Figure 17: Value of C_P along the centerline for the two simulations.

Figures 18, 19, 20, 21 show the total pressure coefficient on different planes in the streamwise direction, which can help with the identification and the analysis of the vortices generated. On the cutting plane just downstream of the front wing (Figure 18) three counterclockwise vortices located around the endplate can be found: on the top edge, near the canard position and on the lower edge. All these vortices can be generated either because of the boundary layer separation or due to the pressure difference on the edges of the body. On the plane $x = 1.25$ m (Figure 19) an inboard vortex, located near the lower portion of the tyre, is well defined. It comes from the jetting phenomenon, explained in Section 1.1, and it is interacting with the lower edge vortex of the endplate. The outboard vortex, which is generated by the same effect, is smaller and it is still not well defined on this plane. Moreover, the upper edge and canard vortices of the endplate are still relatively small, and they will be more prone to instabilities and breakdown. The plane $x = 1.7$ m (Figure 20) is located just downstream the tyre. It is visible the vortex that is formed from the summation of the lower edge endplate vortex and the inboard one coming from the tyre. It is possible to observe also the pair of counter-rotating vortices generated by the wheel shoulders, which were visible also in the isolated tyre case (Figure 14). The major difference with the isolated wheel case is in the lower region of the wake, where it is no longer possible to distinguish the pair of ground vortices. The presence of the front wing, hence the interaction with the vortices generated has led to changes in behavior of the flow, with a consequence also on the aerodynamic coefficients.

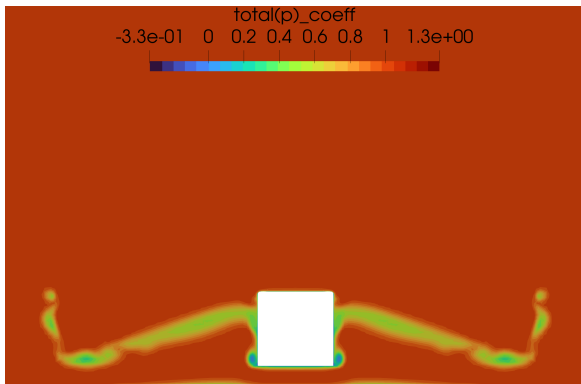


Figure 18: C_{Ptot} at $x = 0.9$ m.

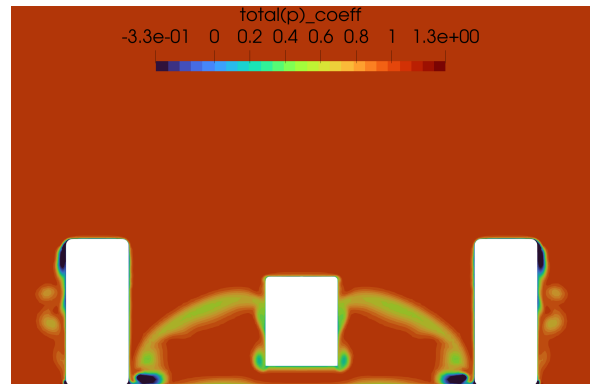


Figure 19: C_{Ptot} at $x = 1.25$ m.

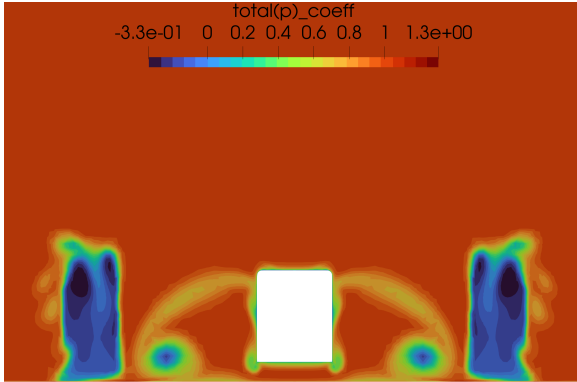
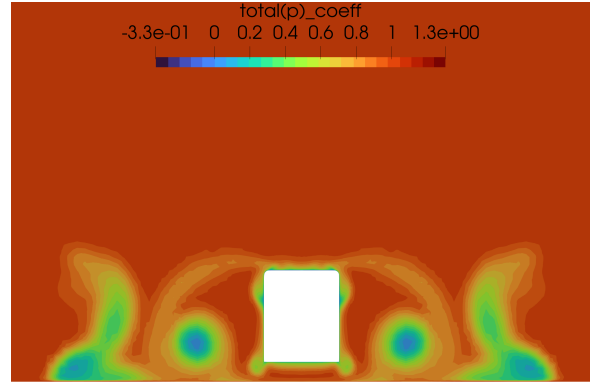
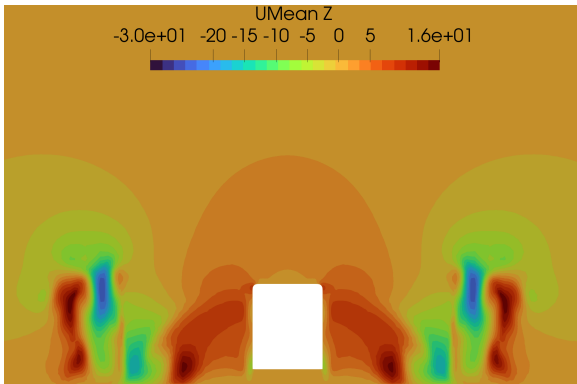
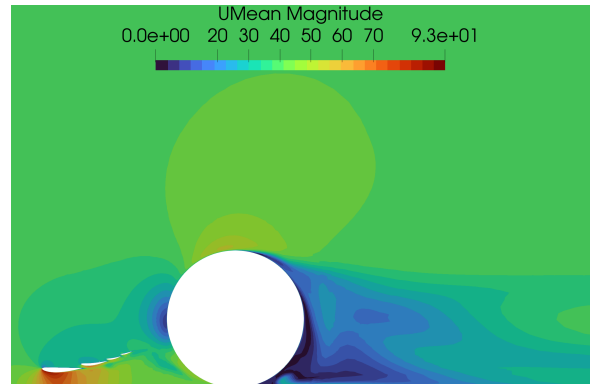
Figure 20: C_{Ptot} at $x = 1.7$ m.Figure 21: C_{Ptot} at $x = 2.5$ m.

Figure 21 shows the plane $x = 2.5$ m, where the vortex generated by the interaction between wing and tyre is still well defined, whereas the wake of the wheel is keeping the same shape. For a more in depth analysis of the tyre wake, the vertical velocity component is shown in Figure 22, which allows to find regions of upwash and downwash, offering a better overview of the behavior of the flow in the wake region. With respect to the isolated wheel case, because of the different behavior of the top vortices, the strong downwash is no longer present, which is coherent with the plot of the C_{Ptot} in Figure 21.

Figure 22: Vertical velocity component at $x = 1.7$ m.Figure 23: Mean velocity magnitude on the wheel centerline (plane $y = 0.98$ m).

5. Conclusion

In this last section, all the relevant results emerged from this study are gathered. This work presented an analysis of the wake of a wheel, in both the isolated case and when the presence of a front wing is considered. Keeping in mind all the limitations related to steady-state RANS simulations when dealing with a problem which has a strong unsteady behavior, this study is still able to present a detailed topology of the wake of an isolated tyre.

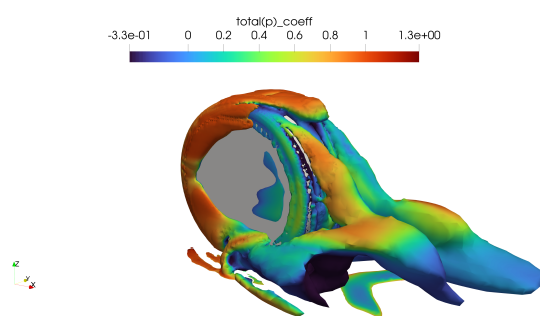


Figure 24: Q-criterion visualization for isolated wheel.

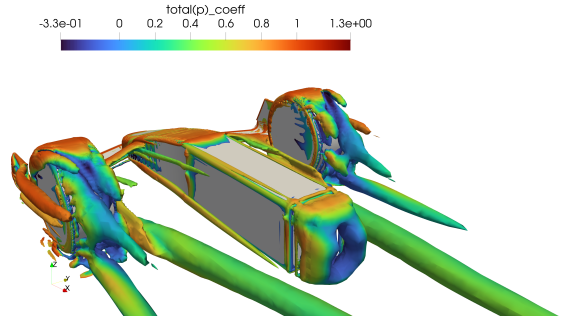


Figure 25: Q-criterion visualization for wing and tyre.

Figures 24 and 25 allow the identification and visualization of the vortices with the Q-criterion, the threshold has been set arbitrarily to 5000 s^{-2} . The vortices identified are coherent with previous experimental and numerical studies present in literature [3], [6], [7]. When also the front wing is considered, the behavior of the flow is significantly affected. This analysis is crucial to understand how it is possible to control the wheel wake through the design of the wing. With the introduction of the 2022 technical regulations, the endplate appears to be a fundamental element, due to the vortical structures. In particular, the vortex generated from the interaction between the lower edge endplate vortex and the wheel ground one seems to be pivotal in dictating the behavior of the flow field. Regarding the influence of the wing on the wheel aerodynamics, a different distribution of the C_P on the centerline of the tyre has been found, with the stagnation point being moved upwards by $\approx 4^\circ$, as shown in Figure 27, while the flow separation occurs before, since the detachment point has been displaced upwards by $\approx 9^\circ$.

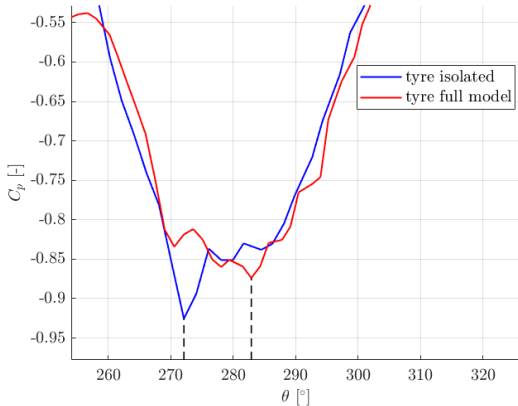


Figure 26: Zoom on the separation point.

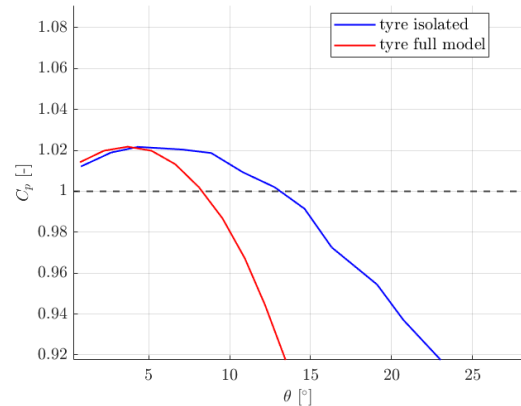


Figure 27: Zoom on the stagnation point.

Lastly, the aerodynamic coefficients are presented in Table 7, the lift coefficient has been reduced by the 41.25%, enhancing the performance of the car and increasing the level of grip. The C_D shows a reduction of the 57.82%,

	$C_{L_{\text{wheel}}}$	$C_{D_{\text{wheel}}}$
Isolated Model	0.4766	0.6630
Full Model	0.2800	0.2796

Table 7: Aerodynamic coefficients on the wheel.

References

- [1] Fédération Internationale de l’Automobile. *2022 Formula 1 Technical Regulations*.
- [2] B. Agathangelou and M. Gascoyne. Aerodynamic design considerations of a formula 1 racing car. *SAE Technical Paper 980399*, 1998.
- [3] John E. Fackrell. The aerodynamics of an isolated wheel rotating in contact with the ground. 1974. URL <https://api.semanticscholar.org/CorpusID:114862502>.
- [4] Alexander Wäschle. The influence of rotating wheels on vehicle aerodynamics - numerical and experimental investigations. 2007. URL <https://api.semanticscholar.org/CorpusID:106672244>.
- [5] F. R. Menter. Two-equation eddy-viscosity turbulence models for engineering applications. *AIAA Journal*, 32:1598–1605, 1994.
- [6] Jacques Heyder-Bruckner. The aerodynamics of an inverted wing and a rotating wheel in ground effect. 2011. URL <https://api.semanticscholar.org/CorpusID:107761720>.
- [7] Dipesh Patel, Andrew Garmory, and Martin Passmore. On the wake of an isolated rotating wheel: An experimental and numerical investigation. *Journal of Wind Engineering and Industrial Aerodynamics*, 227: 105049, 2022. ISSN 0167-6105. doi: <https://doi.org/10.1016/j.jweia.2022.105049>.